(Received 30 December 2024, Accepted 13 February 2025, Scheduled 21 February 2025)

A Miniaturized UWB MIMO Antenna Design for 5G Multi-Band Applications

Shanhua Yao, Xiaorong Qiu*, and Tianchu Yang

School of Electrical and Information Engineering, Anhui University of Science and Technology, Huainan 232001, China

ABSTRACT: In this paper, an ultra-wideband (UWB) multiple-input multiple-output (MIMO) antenna covering the n77, n78, n79, and 6 GHz bands is proposed for 5G applications, which achieves the full coverage of the 5G NR (New Radio) band with a compact geometry. The antenna is fabricated from low-cost printed circuit boards, with the dimensions of 36 mm × 53 mm × 1.6 mm. The MIMO antenna has been designed with two positive octagonal antenna monopole elements, which feature triangular fractal slots and a defected ground plane. Each of these elements is excited by a microstrip feed, and the antenna operates within a bandwidth of 2.92–16.97 GHz, which encompasses the entire UWB frequency range. The utilization of a floor with T-shaped slots and T-shaped stubs serves to minimize the generation of coupling currents between the antenna elements, thereby achieving an isolation of in excess of 19 dB across the entire operating band and a figure in excess of 20 dB in multiple 5G bands. In addition, simulations and measurements show that the antenna has an envelope correlation coefficient (ECC) less than 0.005, a diversity gain (DG) more than 9.98, a total active reflection coefficient (TARC) less than −30 dB, and a channel capacity loss (CCL) less than 0.3 bit/s/Hz in the operating frequency band, with good gain and stable radiation characteristics. The designed antenna has the potential for significant applications in 5G wireless communications.

1. INTRODUCTION

The fifth generation (5G) of communication technology has become the most widely used communication method in the present era. In comparison with the fourth generation (4G) system, 5G communication is favored by people for providing ultra-dense connections, a Gbps data rate, a low latency of milliseconds and high reliability. Antennas are devices that enable the transmission and reception of signals. Consequently, research on 5G antennas has become a current area of interest. The high cost of millimeter-wave devices and the susceptibility of millimeter-wave signals to environmental interference have prompted researchers to focus on 5G antennas operating in the sub-6 GHz frequency band. The primary operating frequency bands for 5G systems below 6 GHz are n77 (3.3–4.2 GHz), n78 (3.3–3.8 GHz), and n79 (4.4–5 GHz). Furthermore, the Ministry of Industry and Information Technology of the People's Republic of China (MIIT) divided the 6 GHz frequency band (6.425–7.125 GHz) for 5G communications in 2023 [1]. This new 5G communications band is being developed. The advent of sophisticated 5G wireless devices has necessitated the development of compact, multifunctional antennas capable of accommodating the diverse requirements of multiple application scenarios. Compared with narrowband and broadband technologies, UWB technology is characterized by high transmission data rates, low power consumption, and high data security. However, most antennas can only cover the low frequency band of the limited 5G frequency band, and UWB technology has become one of the key technologies for 5G cellular communication in order to cover the 5G frequency band of 6 GHz and below 6 GHz. The frequency band range of UWB antennas specified by the U.S. Federal Communications Commission (FCC) is 3.1–10.6 GHz [2].

Although single-antenna UWB systems are susceptible to multipath effects, the integration of UWB technology with MIMO antenna systems effectively mitigates this issue, leading to enhanced transmission efficiency and communication capacity of the antenna. Nevertheless, in the context of MIMO antenna design, the measurement of isolation represents a crucial metric for assessing diversity [3, 4]. In order to address the issue of coupling, researchers have conducted comprehensive research on 5G MIMO antennas. Ref. [5] employs a trident patch with a defected floor to achieve dual bands for 5G. Rectangular stubs are placed between the antenna elements with isolation below −16 dB, and the bandwidth contains part of the 5G band. Ref. [6] describes a 5G dual-band MIMO antenna that achieves an isolation of −26 dB by incorporating three rectangular slots and a T-shaped stub in the floor, but the bandwidth covers only part of the 5G band. As presented by Xi et al., a compact MIMO antenna is described using an E-shaped patch and an arrow-shaped feed line. A neutral line with a three-quarter circle is used on the floor to improve isolation and expand the bandwidth. The isolation of the antenna is −15 dB at 2.28–2.7 GHz and 4.96–6.1 GHz [7]. Ref. [8] describes a MIMO antenna in Ro5880 material using nine circular radiators with embedded rectangular slots, enabling the antenna to achieve a bandwidth of 2.3–11.5 GHz, while −16 dB isolation between the units is achieved through rectangular slots. According to Zeain et al.'s 2024 work, a compact MIMO antenna that uses triangular slots and parasitic cells between the antenna elements to reduce the

* Corresponding author: Xiaorong Qiu (2023200719@aust.edu.cn).

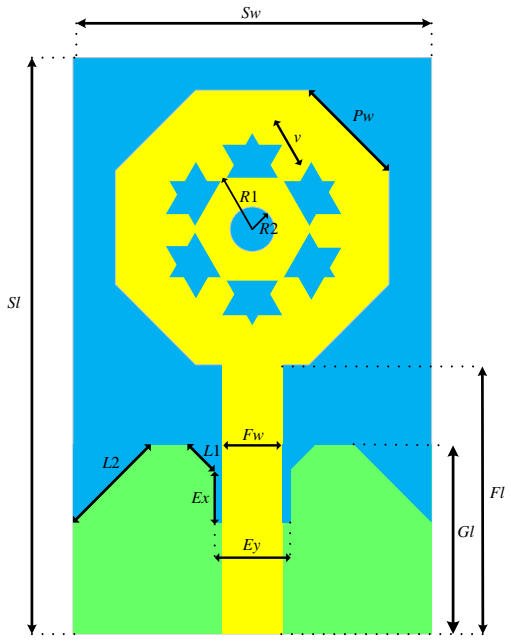

FIGURE 1. Single-element antenna structure.

coupling between the two ports is described. However, the antenna's isolation at 3–6 GHz is −13 dB [9].

A four-port rectangular patch MIMO antenna is presented in [10]. The antenna elements are placed orthogonally to reduce the coupling between the elements so that the isolation between the ports is less than −21 dB, and the antenna has a relatively large size of $60 \times 60\,\text{mm}^2$. Ref. [11] describes a reconfigurable MIMO antenna for 4G and early 5G applications. The antenna consists of two meandering radiating arms diagonally opposite to each other, achieving isolation below −12 dB. The overall size is $120 \times 60\,\text{mm}^2$, which is relatively large. As presented by Kumar et al., a compact MIMO antenna is introduced that uses a neutralization line as a decoupling structure. This antenna employs circular and rectangular embedded radiators along with defected ground structures to access the UWB spectrum, and the neutralization line structure enables it to operate with a bandwidth isolation of less than −16 dB [12]. In [13], a two-port circular MIMO antenna was designed. A T-shaped stub with rectangular grooves was incorporated into the ground plane of the antenna to reduce the convergence of coupling currents and to achieve an isolation of less than −22 dB. Ref. [14] describes a reconfigurable UWB MIMO antenna. T-shaped stubs and stepped rods are used above the antenna floor, and the isolation of the antenna is below −30 dB. In Islam et al.'s work in 2022, a reconfigurable MIMO antenna is described using a band-stop filter as its decoupling structure, achieving an isolation below −20 dB across the entire operating bandwidth, which spans 2.43–2.60 GHz and 3.51–3.79 GHz [15]. As detailed in [16], a two-port MIMO antenna with self-isolation is proposed, which utilizes pattern cancellation techniques to achieve a self-decoupling mechanism. The antenna has more than 22 dB of isolation over the operating bandwidth. Despite the various decoupling techniques proposed in the existing literature to mitigate the coupling effect, the designed antenna still exhibits shortcomings in other performance metrics. These include an increased antenna size, incomplete coverage of the operating bandwidth, a resonance point that is not aligned with the applied frequency band, a lack of minimization of coupling between antenna elements, and a need for improvements in peak gain and radiation efficiency.

Based on the above scheme, this paper presents a novel miniaturized antenna structure and design methodology with a planar profile, compact size, enhanced bandwidth and performance, and high isolation characteristics for 5G applications in the n77, n78, n79 and 6 GHz bands. In addition, the antenna employs a defected ground structure with T-shaped stubs to reduce the coupling effect between the ports and improve the impedance matching in the operating band, as well as optimizing the location of the resonance points without the need for more complex decoupling structures. The final operating bandwidth of the designed antenna is 2.92–16.97 GHz, and the resonance points are in the n77, n78 and 6 GHz bands of 5G. The antenna exhibits good gain, directivity, ECC, and CCL characteristics in professional bandwidth applications, including those related to 5G technology.

2. SINGLE-ELEMENT ANTENNA DESIGN

2.1. Cell Antenna Structure

The geometry of the monopole antenna designed in this paper is shown in Figure 1. The antenna is made of an FR4 substrate with a thickness of 1.6 mm, which has a relative dielectric constant (ε_r) of 4.4, a loss tangent ($\tan\delta$) of 0.02, and an overall physical size of 32 mm × 22 mm. The front of the baseplate consists of a square octagonal radiator and a rectangular microstrip feed line with an etched triangular fractal slot and embedded nut ring placed in the center of the radiator, allowing the signal from the antenna to radiate freely. The backside of the substrate uses a partial floor and rectangular slots, with corners cut on each side of it respectively, as a way to improve the impedance matching of the antenna. The antenna design is simulated and optimized using HFSS2023R1 software to determine the antenna structure, and the final geometry of the designed antenna is shown in Table 1.

TABLE 1. Dimensions of single-element antenna structures.

Parameters	***Sw***	***Sl***	***Fw***	***Fl***	***Gl***	***Pw***	***V*1**
Value (mm)	22	32	3	11	13.8	6.2	2.9
Parameters	***V*2**	***L*1**	***L*2**	***R*1**	***R*2**	***Ex***	***Ey***
Value (mm)	8.7	1	3.2	4.5	1.5	4.5	3.5

2.2. Stages of Antenna Design Evolution

The conventional rectangular monopole is modified to obtain an operating bandwidth in the UWB range and to ensure a resonant response at 5G frequencies. The evolution of the antenna structure is shown in Figure 2 and is divided into six steps, with the S_{11} parameter curves for each stage shown in Figure 3.

In the first step, a rectangular microstrip antenna as shown in Figure 2(a) is designed from Equations (1)–(4), and c is the

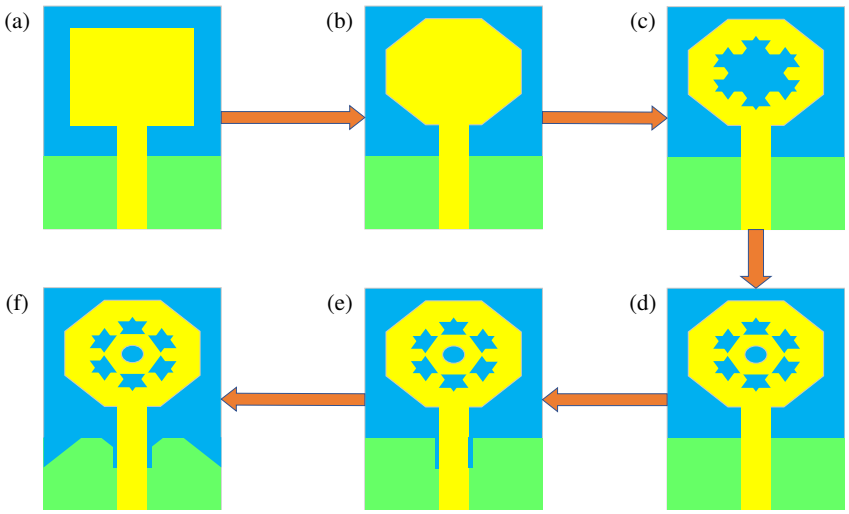

FIGURE 2. Design flow of monopole antenna: (a) Ant 1, (b) Ant 2, (c) Ant 3, (d) Ant 4, (e) Ant 5, (f) Ant 6.

speed of light in air, f the frequency, L the length of the patch, w its width, h the thickness of the substrate, and ε_r the effective dielectric constant of the medium. Generally, the design phase begins with the selection of the lowermost operational frequency for the antenna. Typically, the lower frequency of the antenna operation depends on both maximum antenna size and effective dielectric constant (ε_{eff}) of the material. Consequently, antenna width (w) and length (L) are calculated using Equations (1)–(4). As shown by the black line in Figure 3, the antenna produces a narrow bandwidth of operation in the low frequency band of 5G and resonates at the 5G frequency point of 3.6 GHz.

$$L = \frac{c}{2f\sqrt{\varepsilon_{eff}}} - 2\Delta L \tag{1}$$

$$\Delta L = 0.412h\frac{(\varepsilon_{eff}+0.3)\left(\frac{w}{h}+0.262\right)}{(\varepsilon_{eff}-0.258)\left(\frac{w}{h}+0.813\right)} \tag{2}$$

$$\varepsilon_{eff} = \frac{\varepsilon_r+1}{2} + \frac{\varepsilon_r-1}{2}\left(1+\frac{12h}{w}\right)^{-\frac{1}{2}} \tag{3}$$

$$w = \frac{\lambda_0}{2}\left(\frac{\varepsilon_r}{2}\right)^{-\frac{1}{2}} \tag{4}$$

In the second step, the four corners of the rectangle on the front side of the antenna are cut, creating a positive octagonal radiator. This design allows the current to flow more smoothly over the surface of the patch due to the gradual change in the edge corners. As a result, the frequency near the center frequency point meets the resonance requirements, improving the impedance matching of the antenna. Consequently, the bandwidth of the low frequency band is expanded, as shown in Figure 2(b).

In the third step, the radiating patch is grooved in order to further increase the bandwidth of the antenna. The introduction of the triangular fractal groove interferes with the surface charge distribution of the radiating patch, reducing the convergence of the current in the center of the patch and allowing the antenna to support multiple resonances. The antenna structure is illustrated in Figure 2(c). It demonstrates that the antenna generates four distinct resonance points, effectively expanding the bandwidths of both the low and high bands as illustrated by the green curves in Figure 3.

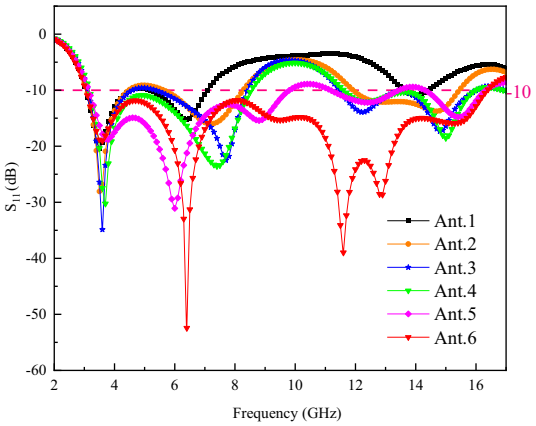

FIGURE 3. Simulation results of six antennas.

In the fourth step, as illustrated in Figure 2(d), a nut ring is incorporated within the fractal slot of the antenna. The radius of the circle is calculated and verified by Equations (5)–(7). The current path generated by the nut ring serves to augment the resonant response of the antenna and enhance impedance matching, resulting in reflection coefficients of less than -10 dB from 3 GHz to 8 GHz. F_{rc} represents the circular undercut of the resonant frequency in terms of GHz.

$$R = T\left[1+\frac{2h}{\pi T\varepsilon_r}\left(\ln\left(\frac{\pi T}{2h}\right)+1.7726\right)\right]^{-\frac{1}{2}} \tag{5}$$

$$T = \frac{8.719\times10^9}{\sqrt{\varepsilon_r}F_{rc}} \tag{6}$$

$$F_{rc} = \frac{c}{2\pi R\sqrt{\varepsilon_{eff}}} \tag{7}$$

In the fifth step, the floor is slotted in order to improve the impedance matching of the antenna, as shown by the green curve in Figure 3. The introduction of the rectangular slot in the floor reduces the overall reflection coefficient of the antenna, especially in the lower frequency bands, thus enhancing the impedance matching. As a result, a significant breakthrough is made in order to achieve UWB performance of the antenna.

In the sixth step, in order to ensure that the antenna's operational bandwidth encompasses the entire UWB frequency range, the floor rectangular slot and floor edge are subjected to corner cutting, resulting in the antenna structure depicted in Figure 2(f). The final result coefficients are represented by the red curve in Figure 3. It can be concluded from the curve that the antenna working bandwidth is 3.04–16.39 GHz, with resonance points occurring at 3.6 GHz, 6.4 GHz, 11.6 GHz, and 12.8 GHz, respectively. The antenna meets the design objectives of having a UWB operating band and generating resonance points in the 5G frequency range with good reflection coefficient values.

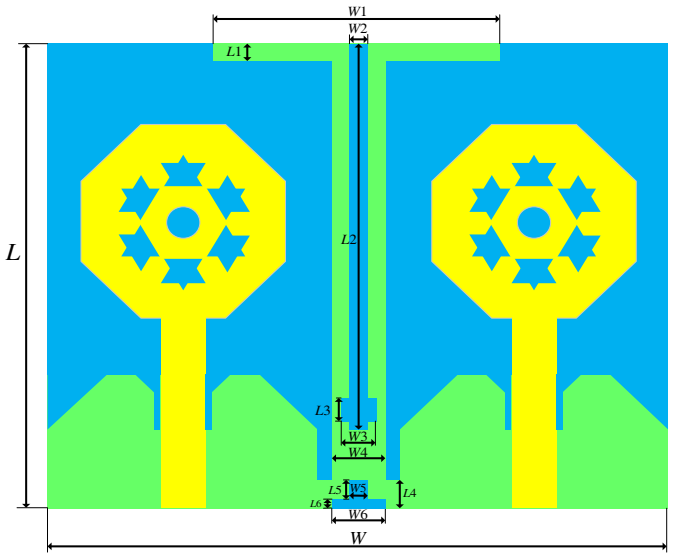

FIGURE 4. UWB MIMO antenna structure.

3. MIMO ANTENNA DESIGN

3.1. Antenna Structure

The design of the MIMO antenna is shown in Figure 4. The antenna uses an FR4 substrate with dimensions of 36 mm × 53 mm × 1.6 mm. The antenna consists of two symmetrical monopole radiator patches fed with a 50 Ω microstrip line. Since the coupling between the monopoles depends on the distance between the radiators, the design aims to ensure a high degree of isolation between the antenna ports while simultaneously reducing the size of the substrate. As a result, a T-shaped stub is introduced in the middle of the antenna's ground plane. Additionally, a hammer-shaped slot is etched in the middle of the T-shaped stub, and an inverted T-shaped slot is positioned at the bottom of the ground plane. These modifications not only help to reduce the coupling currents between the antenna ports but also improve the reflection coefficient and trigger multiple resonance responses. The structural dimensions of the designed antenna are shown in Table 2.

TABLE 2. Dimensions of the MIMO antenna structure.

Parameters	W	L	$W1$	$W2$	$W3$	$W4$	$W5$
Value (mm)	53	36	27	1.5	3.5	5.6	2.5
Parameters	$W6$	$L1$	$L2$	$L3$	$L4$	$L5$	$L6$
Value (mm)	6	1.5	26	2	4	3	1

3.2. Stages of Antenna Design Evolution

To investigate the function of the decoupling structures and optimize them for good 5G frequency response and high isolation performance in the 5G MIMO antenna, the design evolution of the decoupling structure is shown in Figure 5. Figure 6, on the other hand, presents the S-parameters versus frequency for the four decoupling structures of the antenna. In the initial step of the design process, Figure 5 (Step-1) shows the MIMO antenna without a decoupling structure. The two monopoles are connected via a rectangular strip, resulting in good performance in the low frequency band; however, in the high frequency band, the coupling between antenna elements increases significantly due to the shorter wavelength of electromagnetic waves. The black curve in Figure 6 indicates that this antenna experiences high coupling within the frequency range of 3.07–16.19 GHz. To solve this problem, the second step introduces a T-stub. The T-stub acts as an effective decoupling structure that can reduce the coupling between antenna elements by changing the propagation path and phase of the electromagnetic wave. The green curve in Figure 6 shows that although the overall isolation is improved, the problem of low isolation still exists in the 6–8 GHz range. This is because the size and position of the T-stub are not optimized to the best, or the electromagnetic wave propagation characteristics do not interact sufficiently with the T-stub in this frequency band.

In the third step, hammer-shaped slots were designed to enhance isolation within the mid-frequency band. The hammer-shaped slots can further change the propagation path and phase of electromagnetic waves to achieve better isolation in the mid-frequency band. However, as shown in the blue curve in Figure 6, while the isolation and bandwidth in the 6–8 GHz range are improved, the isolation at 5.5 GHz is slightly reduced. This is due to the introduction of the hammer slot which has some effect on the antenna's radiation characteristics in this band.

Finally, in the fourth step, an inverted T-slot was used. As a more complex decoupling structure, the inverted T-slot can achieve better overall isolation by controlling the propagation and scattering of electromagnetic waves more finely. The red curve in Figure 6 shows that the overall isolation of the antenna is further improved, and the overall isolation coefficient is lower than −19 dB, which shows the effectiveness of the inverted T-slot in improving the isolation performance of the antenna.

The final antenna operating bandwidth spans from 2.92 to 16.97 GHz, as illustrated in Figure 6(a), with resonance points

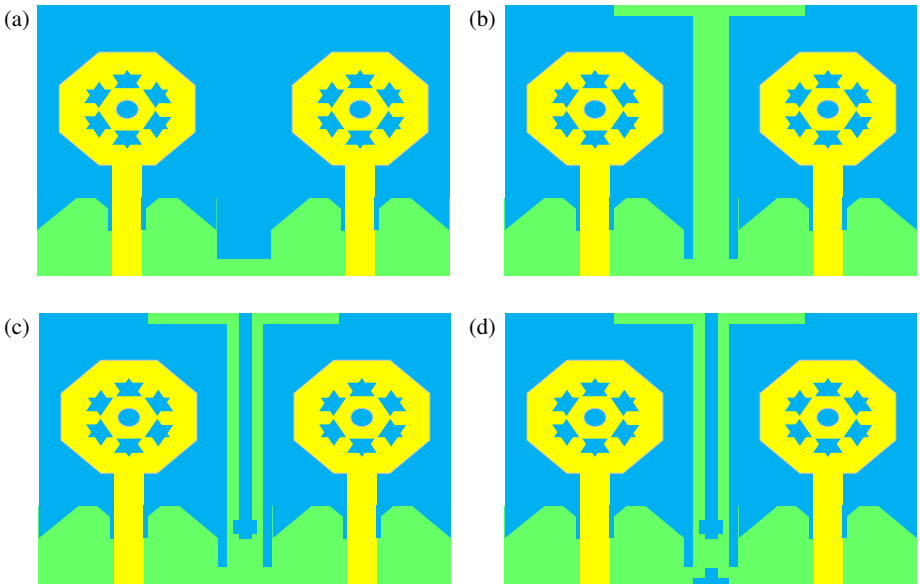

FIGURE 5. Design flow of UWB MIMO antenna: (a) Step-1, (b) Step-2, (c) Step-3, (d) Step-4.

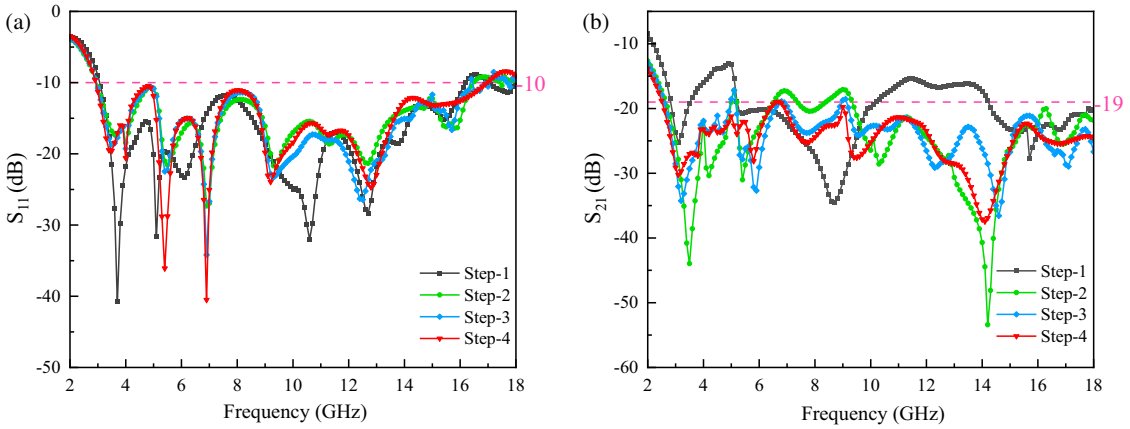

FIGURE 6. Simulation results for antenna 1 to antenna 4: (a) S_{11}, (b) S_{21}.

occurring at 3.5 GHz, 4 GHz, 5.4 GHz, 6.9 GHz, 9.2 GHz, and 12.8 GHz, respectively. As depicted in Figure 6(b), the isolation coefficients within the operating frequency bands are below -20 dB, with an exception in the range of 6.38–6.92 GHz where the isolation coefficient slightly exceeds this threshold.

3.3. Antenna Parameter Analysis

The rectangular groove depth at the antenna floor base and the T-shaped stub dimensions in the middle are crucial in determining the antenna's isolation and reflection coefficient. To optimize the antenna's performance, detailed modelling and parameter tuning were carried out using HFSS simulation software. This process involved optimizing the parameter $W1$ for the T-shaped stub and the parameter $L4$ related to the groove to select the optimal values. As shown in Figure 7(a), varying parameter $W1$ has a negligible impact on the antenna's bandwidth. However, it does have a discernible impact on the resonance point of the low-frequency band. When the value of $W1$ is set to 27 mm, it generates a resonance at 4 GHz, and the up and down of the value of $W1$ will result in the frequency detuning or weakening of the resonance strength. As shown in Figure 7(b), the value of $W1$ also influences the isolation between the antenna elements. The S_{21} value of the antenna is observed to decline as the value of $W1$ increases, and the optimal antenna isolation is attained when the value of $W1$ is 27 mm. As shown in Figure 8, the S_{11} value of the antenna exhibits an increase with the increase of $L4$, whereas the S_{21} value demonstrates a decline with the rise of $L4$. By comparing Figures 8(a) and (b), it is evident that the antenna achieves optimal operating bandwidth and isolation when the value of $L4$ is 4 mm.

3.4. Antenna Current Analysis

To observe the decoupling effect of the antenna isolation structure more intuitively, Figure 9 depicts the surface current distributions of four decoupling structures. By analyzing the surface current relationship between the two antenna elements, im-

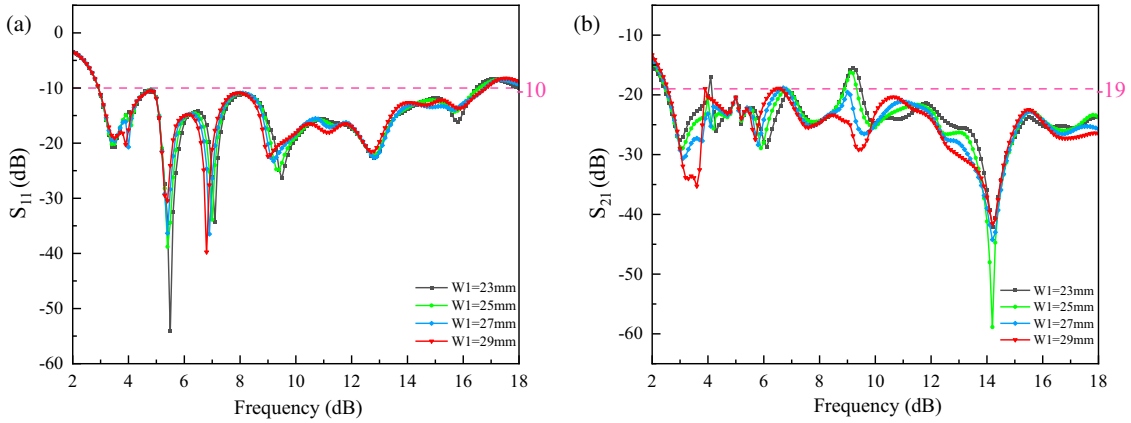

FIGURE 7. Effect of $W1$ parameters on antennas S_{11} and S_{21}: (a) S_{11}, (b) S_{21}.

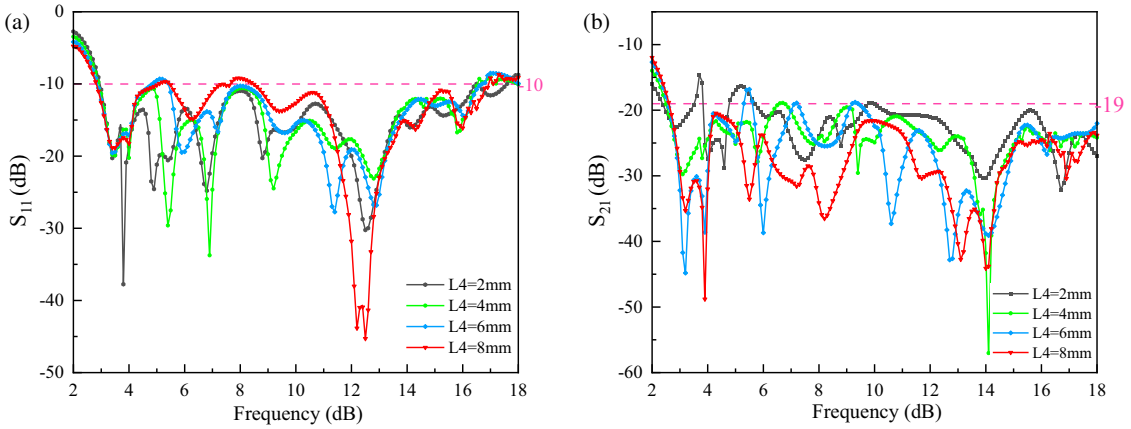

FIGURE 8. Effect of $L4$ parameters on antennas S_{11} and S_{21}: (a) S_{11}, (b) S_{21}.

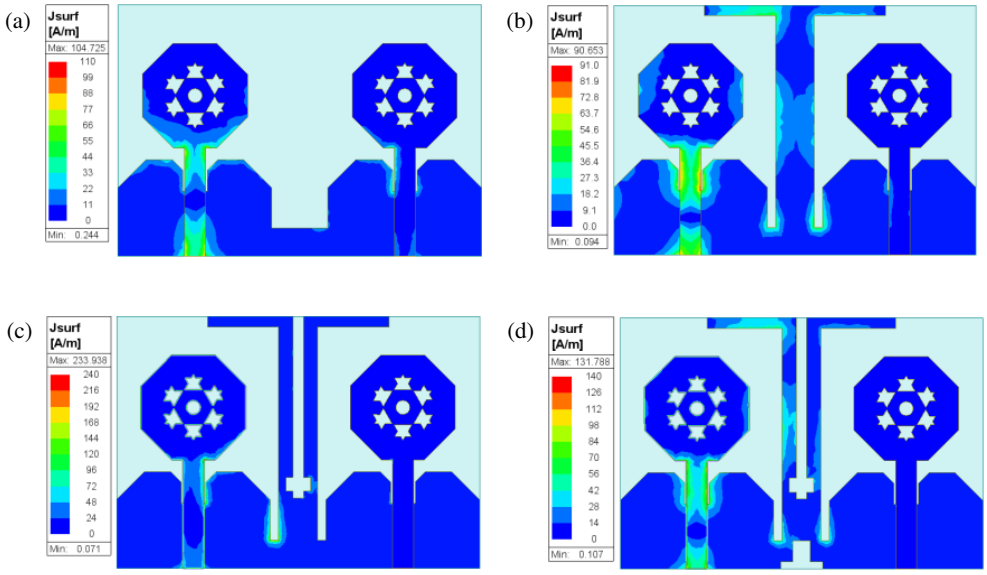

FIGURE 9. Surface current of the antenna: (a) Step-1, (b) Step-2, (c) Step-3, (d) Step-4.

provements can be made to reduce the coupling effect between them. As shown in Figure 9(a), the MIMO antenna consists of two antenna elements interconnected through a rectangular patch on their respective grounds. When antenna port 1 is excited while port 2 remains unchanged, a significant amount of coupling current can be observed on the microstrip line of port 2 using HFSS software for current simulation. In Figure 9(b), a T-shaped stub is added to the ground plane to reduce antenna

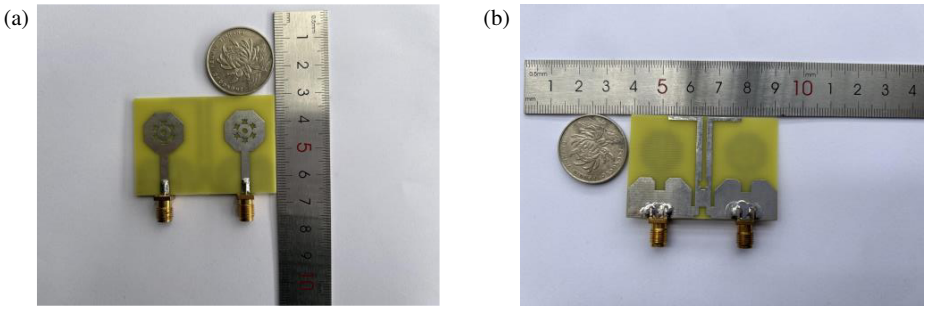

FIGURE 10. MIMO antenna fabrication prototype: (a) front of the antenna, (b) back of the antenna.

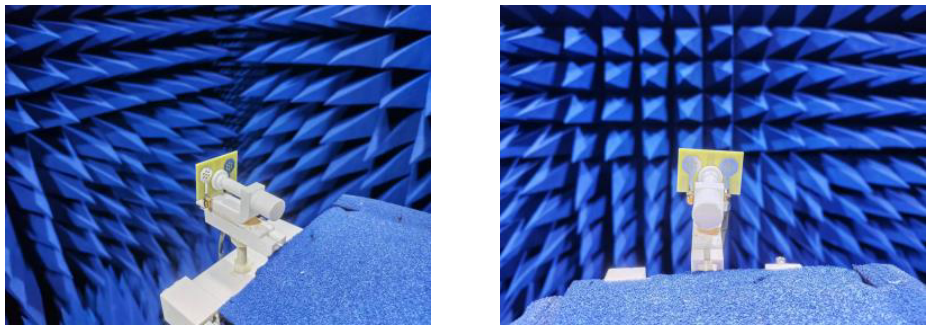

FIGURE 11. Antenna test environment.

coupling, resulting in a notable reduction of coupling current at port 2. Subsequently, in Figure 9(c), a hammer-shaped slot is introduced in the middle of the T-stub to mitigate current stagnation and prevent the current on the T-stub from coupling to port 2. However, a small amount of coupling current still persists in the rectangular slot on the ground plane of port 2. In Figure 9(d), an inverted T-shaped slot is utilized at the bottom of the ground plane. This design directs part of the current to the bottom of the ground plane, causing the coupling current at port 2 to disappear. Consequently, the isolation between the antenna elements is significantly improved. Therefore, the antenna ultimately adopts the decoupled structure shown in Figure 9(d), which effectively blocks current coupling between the antenna ports and achieves a high isolation effect.

4. RESULTS AND DISCUSSION

4.1. *S*-Parameters

To verify the feasibility of the antenna, it was simulated using HFSS software, and the antenna model is physically processed, and the resulting prototype is shown in Figure 10. As shown in Figure 11, the antenna was tested using an Agilent N52235A analyzer within the frequency range of 2–15 GHz, with the untested frequency bands having no impact on the verification of the main band's performance. Figure 12 demonstrates that the overall trend of the measured data aligns with the simulated ones. The impedance bandwidth of the antenna spans from 2.92 to 16.97 GHz, encompassing the n77, n78, n79, and 6 GHz bands for 5G, as well as the UWB from 3.1 to 10.6 GHz. Furthermore, the antenna's S_{12} parameter remains below -19 dB across all operating bands, dipping below -20 dB specifically within the n77 and n78 bands for 5G. Within the n79 and 6 GHz bands, however, the S_{12} parameter only falls within a range between -19 dB and -20 dB for a limited portion of the spectrum. Despite some discrepancies between the simulated and measured S-parameter data shown in Figure 12, which can be attributed to factors such as manufacturing tolerances and SMA interface losses, the overall consistency between the simulated and measured reflection coefficients confirms the viability of the antenna's performance.

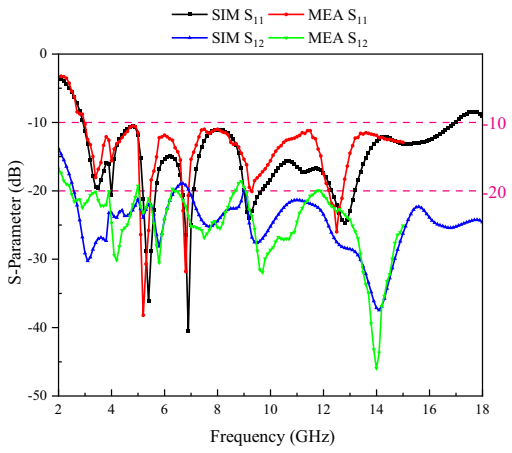

FIGURE 12. Simulated and measured s-parameters.

4.2. Radiation Properties

The far-field radiation pattern of the MIMO antenna was analyzed to verify its far-field characteristics. The radiation in

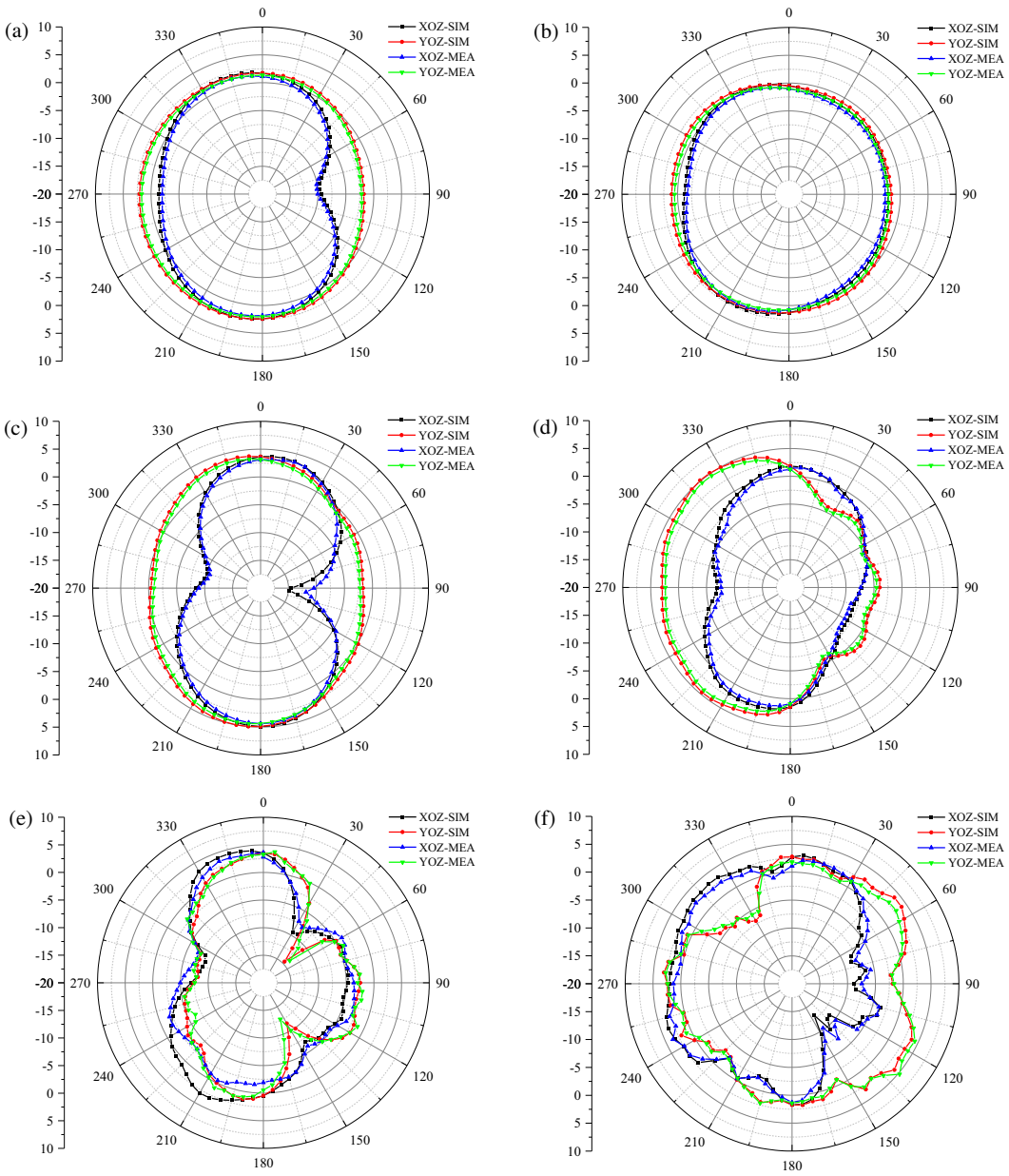

FIGURE 13. Simulated and measured orientation diagrams: (a) 3.5 GHz, (b) 4 GHz, (c) 5.4 GHz, (d) 6.9 GHz, (e) 9.2 GHz, (f) 12.8 GHz.

the XOZ and YOZ planes was measured in a microwave anechoic chamber. The two-dimensional radiation patterns of the resonance points at the test frequencies of 3.5, 4, 5.4, 6.9, 9.2, and 12.8 GHz are shown in Figure 13. From these radiation patterns, it can be observed that the test results generally agree with the simulation ones.

At the resonant frequency of 3.5 GHz, the antenna exhibits bi-directional radiation in the XOZ plane with maximum radiation gain directions at 0° and 180°, while it achieves omnidirectional radiation in the YOZ plane. Figure 13(b) shows that at a frequency of 4 GHz, the antenna achieves quasi-omnidirectional radiation in both the XOZ and YOZ planes.

As shown in Figure 13(c), it can be seen that at a frequency of 5.4 GHz, the antenna radiates bi-directionally in the XOZ plane with maximum radiation directions at 0° and 180°, similar to the pattern at 3.5 GHz, while maintaining omnidirectional radiation in the YOZ plane.

Figure 13(d) indicates that at a frequency of 6.9 GHz, the antenna radiates bi-directionally in the XOZ plane with maximum radiation directions ranging from 0° to 30° and from 180° to 210°. In the YOZ plane, the maximum radiation direction is mainly distributed from 210° to 330°.

At 9.2 GHz, as shown in Figure 13(e), the maximum radiation directions of the antenna in the XOZ plane are concentrated near 315° and 15°, as well as between 180° and 240° (excluding exactly 180° due to a separate peak near that angle). In the YOZ plane, the maximum radiation directions are mainly distributed between 330° and 30° (wrapping around the 0°/360° point) and between 180° and 210°.

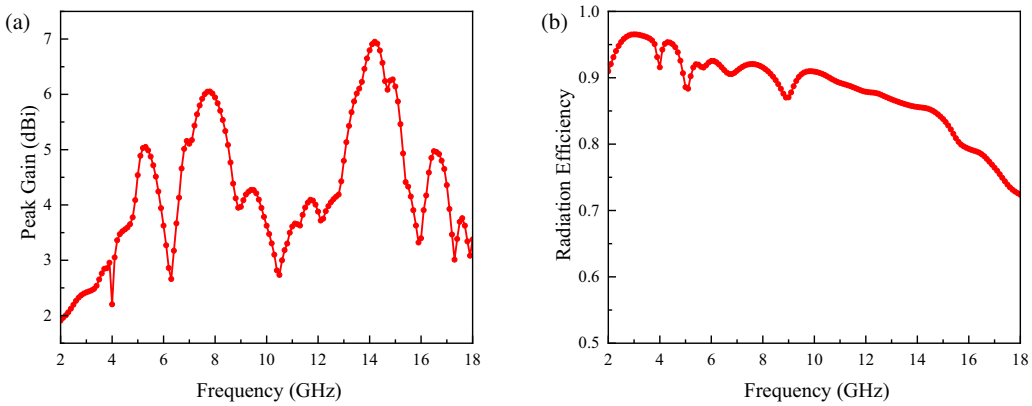

FIGURE 14. Peak gain and radiation efficiency of the antenna: (a) Peak gain, (b) Radiation efficiency.

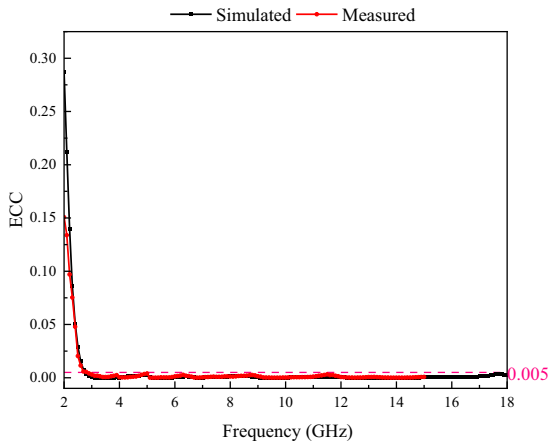

FIGURE 15. Simulated and measured antenna ECCs.

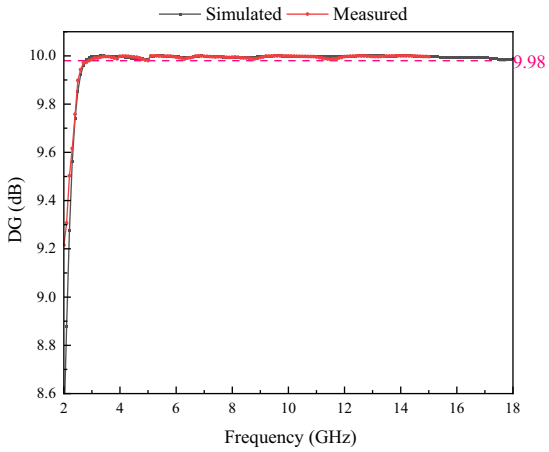

FIGURE 16. Simulated and measured antenna DGs.

Finally, Figure 13(f) shows that at 12.8 GHz, the antenna radiates almost omnidirectionally in both the XOZ and YOZ planes. However, due to the higher frequency, there is some distortion in the radiation pattern in certain directions, which may be attributed to physical effects such as diffraction or interference.

Figure 14 displays the maximum gain and radiation efficiency of the MIMO antenna. As shown in Figure 14(a), the antenna's peak gain (or the maximum gain of the radiation sphere) increases significantly with frequency, reaching a maximum value of 6.95 dBi at a specific frequency point. This is attributed to the enlargement of the radiating patch's electrical size (the ratio of its physical size to the wavelength) as the frequency rises, which enhances radiation efficiency and consequently optimizes the gain performance. In Figure 14(b), the radiation efficiency of the antenna, which represents the antenna's ability to convert current in the conductor into airborne electromagnetic waves, ranges from 73% to 96%. Notably, the radiation efficiency decreases as the frequency increases, due to an increase in resistive loss and a decrease in coupling between the antenna and its surrounding environment. Despite this trend, the radiation efficiency of the antenna within the 5G operating frequency band remains above 90%, with the exception of the n79 band. Overall, the antenna exhibits good radiation performance. Due to limited experimental conditions, measured parameters for gain, radiation efficiency, co-polarisation and cross-polarisation are not yet available.

4.3. MIMO Antennas Performance

4.3.1. ECC and DG

Envelope correlation coefficient (ECC) is an important metric reflecting the isolation or correlation between wireless communication channels as a parametric index for evaluating the diversity performance and coupling performance of MIMO multi-antenna systems. The smaller the value of ECC is, the smaller the influence is between antenna elements, and the better the MIMO antenna performance is. Under the requirements of engineering applications, the acceptable maximum value of ECC for MIMO antenna is 0.5. ECC can be obtained from Equation (7).

$$ECC = \frac{\left|\iint_{4\pi}\left[\overrightarrow{F_1}(\theta,\varphi) * \overrightarrow{F_2}(\theta,\varphi)\right] d\Omega\right|^2}{\iint_{4\pi}\left|\overrightarrow{F_1}(\theta,\varphi)\right|^2 d\Omega \iint_{4\pi}\left|\overrightarrow{F_2}(\theta,\varphi)\right|^2 d\Omega} \quad (8)$$

As shown in Figure 15, the ECC of the antenna is less than 0.005 in the operating band, which indicates that the correlation

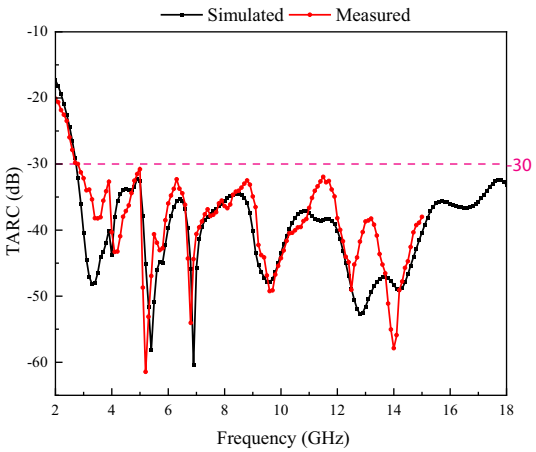

FIGURE 17. Simulated and measured antenna TARCs.

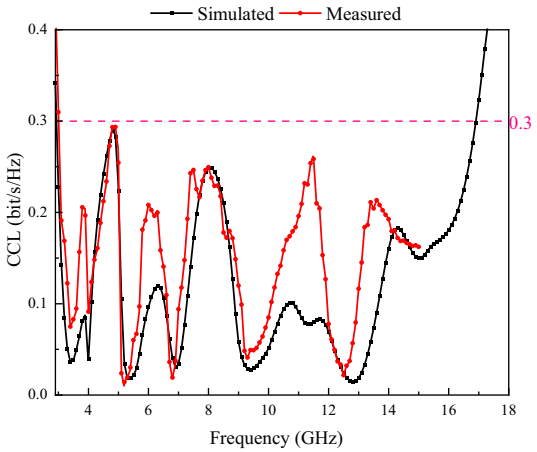

FIGURE 18. Simulated and measured antenna CCLs.

TABLE 3. Comparison of the proposed antenna with several existing antennas.

Ref	Size (mm^2)	Bandwidth (GHz)	Isolation (dB)	ECC	Radiation efficiency (%)
[17]	60×65	3.1–5.1	< -15	< 0.13	70–82
[18]	90×90	2.77–12	< -15	< 0.1	75–82
[19]	60.5×62.5	3.5–11	< -20	< 0.01	70–90
[20]	68×128	3.55–3.8 4.6–4.8	< -14	< 0.04	90–97
[21]	50×50	3.05–11.3	< -16	< 0.02	-
[22]	30×30	1.9–3.6 4.2–11.6	< -18	< 0.07	25–93
[23]	30×40	3.20–5.85	< -17.5	< 0.05	80–88
This Work	**36×53**	**2.92–16.97**	$< \mathbf{-19}$	$< \mathbf{0.005}$	**73–96**

between the antenna elements is very small, and the antenna can work stably in the MIMO system.

Diversity gain (DG) is another performance metric of the MIMO antenna, which can be calculated from the ECC, and the closer its value is to 10 dB, the better the antenna works efficiently. Equation (9) is as follows:

$$DG = 10 \times \sqrt{1 - ECC} \tag{9}$$

As shown in Figure 16, the antenna exhibits a minimum value of DG within the operational band of 9.98 dB, thereby demonstrating favorable diversity performance.

4.3.2. TARC and CCL

Total active reflection coefficient (TARC) is an important performance metric for MIMO antennas. It indicates the effective bandwidth of a MIMO antenna when multiple ports are excited at the same time and can be calculated using the S-parameter. In general, a TARC value less than -10 dB in the frequency band is considered to design an antenna with low reflection loss and good phase stability. Equation (10) for calculating the TARC of the dual-port MIMO antenna is given below:

$$TARC = \sqrt{\frac{(S_{11} + S_{12})^2 + (S_{21} + S_{22})^2}{2}} \tag{10}$$

The TARC curve of the antenna is shown in Figure 17, from which it can be seen that the average TARC measured over the operating band range is less than -30 dB, which indicates that the antenna is insensitive to phase variations, so the MIMO antenna has good performance.

Channel capacity loss (CCL) is also an important parameter of multi-input multi-output antennas, indicating the channel capacity loss of the antenna for transmitting and receiving signals. Generally, the channel capacity loss of the antenna is considered acceptable if the CCL is less than 0.4 bit/s/Hz. The CCL can be calculated by Equations (11), (12), (13), and (14).

$$CCL = -\log_2 det\left(\alpha^R\right) \tag{11}$$

$$\alpha^R = \begin{bmatrix} \alpha_{11} & \alpha_{12} \\ \alpha_{21} & \alpha_{22} \end{bmatrix} \tag{12}$$

$$\alpha_{ii} = 1 - \left| \sum_{n=1}^{2} S_{in} * S_{ni} \right| \tag{13}$$

$$\alpha_{ij} = -\left| \sum_{n=1}^{2} S_{in} * S_{nj} \right| \tag{14}$$

Figure 18 shows the CCL of the antenna, which exhibits a channel loss of less than 0.3 bit/s/Hz across all operating bands, indicating the high reliability of the antenna.

5. COMPARE WITH EXISTING ANTENNAS

Table 3 demonstrates a comparison of the proposed antenna in this paper with several existing antennas in terms of size, bandwidth, isolation, ECC, and radiation efficiency. The proposed antenna is smaller in size than those in [17–21]. It has a wider operating bandwidth than those in [17–23]. It exhibits better decoupling capability than those in [17, 18, 20–23]. The ECC values of the proposed antenna are lower than those in [17–23]. The radiation efficiency of the proposed antenna is higher than those antennas in [17–19, 22, 23], and it basically exceeds 90% in the 5G band. Thus, the antenna proposed in this paper performs well in all aspects.

6. CONCLUSION

In this paper, a compact UWB MIMO antenna is designed with an operating bandwidth of 2.92–16.97 GHz for 5G in n77, n78, n79 and 6 GHz bands, and the antenna is constructed with a novel trapezoidal defected floor structure to obtain the UWB characteristics. T-shaped stubs and T-shaped slots are introduced in the MIMO antenna floor, and the mutual coupling between the antenna ports is resolved by analyzing the current distribution of the model in order to keep the isolation parameter of the antenna below -19 dB in the operating band range. The gain and efficiency of the designed antenna are 6.9 dBi and 90%, respectively, and good radiation patterns are observed in both the E-plane and H-plane at the center frequency. By calculating the performance metrics such as ECC, DG, CCL, and TARC in the operating band, the results show that all the metrics satisfy the industry standards, and the antenna has good MIMO performance. Therefore, due to its good radiation characteristics, diversity performance, and compact size, it has a good application prospect in the field of 5G wireless communication.

ACKNOWLEDGEMENT

This work was partially supported by the National Natural Science Foundation of China (No. 62105004) and the Natural Science Research Program for Universities in Anhui Province (No. KJ2020A0308).

REFERENCES

[1] Ministry of Industry and Information Technology, "Regulations of the People's Republic of China on the division of radio frequencies," 1–241, China, 2023.

[2] Federal Communications Commission, "Ultra-wideband transmission systems," *Federal Register*, Vol. 67, No. 95, 47 CFR Part 15, 34 852–34 860, 2002.

[3] Molisch, A. F. and M. Z. Win, "MIMO systems with antenna selection," *IEEE Microwave Magazine*, Vol. 5, No. 1, 46–56, 2004.

[4] Paulraj, A. J., D. A. Gore, R. U. Nabar, and H. Bolcskei, "An overview of MIMO communications — A key to gigabit wireless," *Proceedings of the IEEE*, Vol. 92, No. 2, 198–218, 2004.

[5] Sharma, P., R. N. Tiwari, P. Singh, and B. K. Kanaujia, "Dual-band trident shaped MIMO antenna with novel ground plane for 5G applications," *AEU — International Journal of Electronics and Communications*, Vol. 155, 154364, 2022.

[6] Wang, W., Y. Wu, W. Wang, and Y. Yang, "Isolation enhancement in dual-band monopole antenna for 5G applications," *IEEE Transactions on Circuits and Systems II: Express Briefs*, Vol. 68, No. 6, 1867–1871, 2021.

[7] Xi, S., J. Huang, B. Chen, and G. Liu, "A compact dual-band multi-input multi-output antenna for 5G/WLAN/Bluetooth applications," *Microwave and Optical Technology Letters*, Vol. 64, No. 2, 325–330, 2022.

[8] Kiani, S. H., H. S. Savci, M. E. Munir, A. Sedik, and H. Mostafa, "An ultra-wide band MIMO antenna system with enhanced isolation for microwave imaging applications," *Micromachines*, Vol. 14, No. 9, 1732, 2023.

[9] Zeain, M. Y., M. Abu, A. A. Althuwayb, H. Alsariera, A. J. A. Al-Gburi, A. A. Abdulbari, and Z. Zakaria, "A new technique of FSS-based novel chair-shaped compact MIMO antenna to enhance the gain for sub-6GHz 5G applications," *IEEE Access*, Vol. 12, 49 489–49 507, 2024.

[10] Abbas, A., N. Hussain, M. A. Sufian, J. Jung, S. M. Park, and N. Kim, "Isolation and gain improvement of a rectangular notch UWB-MIMO antenna," *Sensors*, Vol. 22, No. 4, 1460, 2022.

[11] Pant, A., M. Singh, and M. S. Parihar, "A frequency reconfigurable/switchable MIMO antenna for LTE and early 5G applications," *AEU — International Journal of Electronics and Communications*, Vol. 131, 153638, 2021.

[12] Kumar, P., T. Ali, and M. P. Mm, "Characteristic mode analysis-based compact dual band-notched UWB MIMO antenna loaded with neutralization line," *Micromachines*, Vol. 13, No. 10, 1599, 2022.

[13] Addepalli, T. and V. R. Anitha, "A very compact and closely spaced circular shaped UWB MIMO antenna with improved isolation," *AEU — International Journal of Electronics and Communications*, Vol. 114, 153016, 2020.

[14] Nej, S., A. Ghosh, J. Kumar, and S. Das, "Ultra-wideband MIMO antenna with reconfigurable band notch characteristics and improved isolation," *AEU — International Journal of Electronics and Communications*, Vol. 170, 154849, 2023.

[15] Islam, H., S. Das, T. Ali, T. Bose, S. Kumari, O. Prakash, and P. Kumar, "Bandstop filter decoupling technique for miniaturized reconfigurable MIMO antenna," *IEEE Access*, Vol. 10, 19 060–19 071, 2022.

[16] Kansal, P., A. K. Mandpura, and N. Kumar, "Triple band self-decoupled MIMO antenna pair for 5G communication," *Physica Scripta*, Vol. 99, No. 9, 095532, 2024.

[17] Thangarasu, D., S. K. Palaniswamy, and R. R. Thipparaju, "Quad port multipolarized reconfigurable MIMO antenna for sub 6 GHz applications," *International Journal of Antennas and Propagation*, Vol. 2023, No. 1, 8882866, 2023.

[18] Alharbi, A. G., U. Rafique, S. Ullah, S. Khan, S. M. Abbas, E. M. Ali, M. Alibakhshikenari, and M. Dalarsson, "Novel MIMO antenna system for ultra wideband applications," *Applied Sciences*, Vol. 12, No. 7, 3684, 2022.

[19] Abdelghany, M. A., M. F. A. Sree, A. Desai, and A. A. Ibrahim, "4-port octagonal shaped MIMO antenna with low mutual coupling for UWB applications," *Computer Modeling in Engineering & Sciences*, Vol. 136, No. 2, 1999–2015, 2023.

[20] Chakraborty, S., M. A. Rahman, M. A. Hossain, E. Nishiyama, and I. Toyoda, "A novel dual-band elliptical ring slot MIMO antenna with orthogonal circular polarization for 5G applications," *Heliyon*, Vol. 10, No. 13, e33176, Jul. 2024.

[21] Tadesse, A. D., O. P. Acharya, and S. Sahu, "A five-port integrated planar ultra wideband and narrowband antennas system using excitation switching reconfigurable technique for cognitive radio applications," *Wireless Personal Communications*,

Vol. 131, No. 1, 527–544, 2023.

[22] Sharma, D., R. Kumar, and R. K. Vishwakarma, "Multi-standard planar compact 4-port MIMO with enhanced performance for ISM/5G NR/C/WLAN/X band applications," *Optik*, Vol. 269, 169871, 2022.

[23] Kulkarni, J., A. Desai, and C.-Y. D. Sim, "Wideband four-port MIMO antenna array with high isolation for future wireless systems," *AEU — International Journal of Electronics and Communications*, Vol. 128, 153507, 2021.